Materials Advances

ROYAL SOCIETY OF CHEMISTRY

PAPER

View Article Online
View Journal | View Issue

Cite this: *Mater. Adv.*, 2024, 5, 8638

Doping stimulated ferromagnetic ordering and tailoring of the dielectric properties of $Ba_{1-x}Ce_xTiO_3$†

Rahul Sharma,[ab] Shreya Sinha,[b] Rahul Singh,[b] Saurabh Pathak,* [c] Barsha Borgohain,[d] Noor Jahan*[b] and N. S. Negi[a]

The concurrent integration of ferroelectricity and ferromagnetism in $BaTiO_3$ (BT) introduces a promising paradigm for multifunctional applications. This study delves into the structural, magnetic, and dielectric characteristics of $Ba_{1-x}Ce_xTiO_3$ (BCT) ceramics with Ce substitution varying from 0 to 2%. Notably, BT in its pristine state exhibited weak ferromagnetism at a lower applied magnetic field. However, the introduction of Ce^{3+} led to an augmentation in the M_s values, attributed to the elevated presence of oxygen vacancies. Rietveld analysis of the X-ray diffraction patterns and the Raman spectra of all the samples revealed the unaltered tetragonal structure of BT despite increasing the Ce content to 1.5%. Simultaneously, an increase in the unit cell volume and crystalline size was noted, whereas the tetragonality factor (c/a) diminished with increasing Ce substitution. Field emission scanning electron microscopy (FESEM) analysis highlighted a transition in the average grain size from 738 nm to 899 nm with increasing Ce content. The investigation of dielectric properties showed a proportional reduction in the dielectric constant with increasing Ce concentration. Additionally, dielectric measurements revealed that AC conductivity increased with frequency, and Ce doping further enhanced the conductivity by introducing additional charge carriers. Despite the reduction in the dielectric constant, the minimal dielectric loss made these materials highly suitable for high-frequency applications. This study underscores the significance of Ce incorporation into BT, introducing magnetic behaviour to an otherwise non-magnetic, lead-free BT system. The observed phenomena open avenues for exploring previously limited multiferroic and magnetoelectric properties of BT ceramics, a promising direction in the realm of lead-free ferroelectrics.

Received 7th June 2024,
Accepted 1st October 2024

DOI: 10.1039/d4ma00593g

rsc.li/materials-advances

1. Introduction

The investigation of advanced materials with multifunctional characteristics is the cornerstone of contemporary scientific research, and BT has emerged as a focal point owing to its inherent ferroelectric properties, which are crucial for diverse electronic applications.[1,2] Compared to other ferroelectrics like lead zirconium titanate (PZT) and bismuth ferrite ($BiFeO_3$), BT offers distinct advantages. While PZT exhibits superior piezoelectric properties, its lead content poses environmental concerns. $BiFeO_3$, though multiferroic, suffers from low magnetization and leakage currents. BT circumvents these issues by providing a suitable balance of ferroelectric and dielectric properties without the associated drawbacks. Traditionally devoid of magnetic characteristics, BT has undergone a wary transformation through controlled doping, resulting in a discernible departure from its intrinsic diamagnetic nature.[3] This intentional modification introduces pronounced ferromagnetic properties, establishing a noteworthy contrast with its conventional properties and revealing the distinctive phenomenon of magnetoelectric coupling, which is an intriguing convergence of ferroelectric and ferromagnetic behaviours. The synergistic amalgamation of ferroelectricity and ferromagnetism in doped BT introduces a promising paradigm for multifunctional applications, representing a fundamental shift in the underpinning properties of the material. Multifunctional materials, combining ferroelectric and magnetic properties, offer significant potential for technological advancements in domains such as

[a] *Department of Physics, Himachal Pradesh University, Summer Hill, Shimla 171005, India*
[b] *Department of Physics and Astronomical Science, Central University of Himachal Pradesh, Dharamshala 176215, India. E-mail: noor.jahan@hpcu.ac.in*
[c] *National Creative Research Center for Spin Dynamics and SW devices, Department of Material Sciences and Engineering, Seoul National University, Seoul 151-744, South Korea. E-mail: saurabh.pathak28@gmail.com*
[d] *Department of Physics, Darrang College, Tezpur, Assam, India*

† Electronic supplementary information (ESI) available. See DOI: https://doi.org/10.1039/d4ma00593g

electronics, energy and healthcare. By combining these properties, we can develop innovative solutions for a wide range of applications including sensors, data storage and actuators used in robotics, automation and medical equipment. This convergence pioneers a sophisticated approach to advancing electronic and magnetic devices, necessitating a comprehensive examination of the nuanced interplay between these augmented characteristics.[4]

BT exhibits diamagnetic characteristics in the bulk phase; however, the introduction of transition metal ions such as Fe, Mn, Co, or Ni through substitution at the Ti site in the crystal lattice induces a profound transformation in its magnetic behavior.[5,6] This substitution disrupts the delicate balance of charges and spins within the lattice, generating localized magnetic moments. The partial filling of the d or f orbitals in transition metal dopants introduces unpaired electrons, contributing to magnetic moments that can align in parallel, fostering a ferromagnetic state. In pursuit of this, Dang *et al.* observed that increasing Fe doping at the Ti site alters oxygen vacancies, transforming diamagnetic BT into a ferromagnetic material. The ferromagnetic shift is attributed to the polarization of electron spins drawn towards positive spots created by oxygen vacancies, aligned with the magnetic moments of the substituted Fe ions.[7] In an analogous study, Lin *et al.* found that Fe^{3+} ions at the Ti site strategically filling the pentahedral and octahedral positions induce ferromagnetic properties in Fe-doped BT because of the super-exchange interactions of Fe^{3+} at these sites.[8] Bhowmik *et al.* chemically synthesized $BaTi_{0.5}Mn_{0.5}O_3$ particles which exhibited a subtle ferromagnetic response at low magnetic fields, with a more pronounced indication of ferromagnetic behavior compared to other synthesis routes, including solid-state and mechanical alloying.[9] Nakayama *et al.* conducted *ab initio* total energy calculations for various transition metal dopants utilizing the local spin density approximation. Mn doping has been highlighted as the most promising transition metal dopant for ferromagnetic applications in BT, with notable potential for Cr and Fe doping.[10]

The strategic substitution of Ba with transition metal ions further enhances this effect, creating an environment where ferromagnetism becomes increasingly pronounced. Alkathy *et al.* investigated Ni and Na co-substitution in BT and observed improved magnetic properties. These ceramics exhibited coexisting ferroelectricity and weak ferromagnetism, attributed to the F-center exchange mechanism.[11] In a captivating study, Maikhuri *et al.* revealed ferromagnetism under both scenarios of Fe doping at the A and B sites of BT. In the case of B-site substitution, oxygen vacancy-mediated super-exchange interactions between nearby Fe^{3+} ions were shown to be the source of ferromagnetism, whereas double exchange interactions between Fe^{2+} and Fe^{3+} were responsible for ferromagnetism in A-site doped BT.[12] The interplay between the charge, spin, and crystal structure in transition metal-doped BT is crucial for comprehending the emergence of ferromagnetic properties. This newfound ferromagnetic character of transition metal-doped BT not only broadens our understanding of multiferroic materials but also opens avenues for applications in spintronics, magnetic storage, and other emerging technologies. The ability to manipulate and enhance magnetic properties through controlled doping offers a promising path for tailoring materials with desired functionalities, adding a layer of versatility to the traditional nonmagnetic BT system.[13,14]

Taking into consideration the multifunctionality and multiferroism, it is essential to emphasize the primary requirement for doping materials: they must yield a single phase of BT. The introduction of transition metal doping, particularly Fe doping, into BT has been observed to generate multiphase compounds, resulting in an undesirable reduction in magneto-electric coupling.[15] This observation serves as a motivation to explore alternative options for transition metal-doped BT. Recently, there has been growing interest in modifying BT with rare-earth ions[16–20] because the introduction of rare earth dopants leads to extraordinary enhancements in the properties such as remarkable solubility, low critical temperature (T_c), good dielectric properties, and photorefractive properties of BT ceramics, surpassing the effects of transition metal dopants.[21–23]

Among the rare earth elements, cerium (Ce) stands out as a significantly abundant element with the ability to readily undergo self-oxidation or reduction to Ce^{4+} and Ce^{3+}, respectively, and induces weak ferromagnetism when introduced in small percentages. Additionally, Ce ions have a suitable ionic radius and valence state as Ba^{2+} and Ti^{4+} ions, which facilitates their substitution into the BT lattice without causing significant structural distortions crucial for preserving its ferroelectric properties. This incorporation offers an opportunity to explore and enhance the multiferroic properties of BT, making it a promising material for spintronic and multifunctional devices.[24] It has been reported that Ce, when present in the Ce^{3+} valence state, is captured at Ba^{2+} sites, whereas Ce^{4+} occupies Ti^{4+} sites.[25] Numerous experiments leading to remarkable results have emerged with the introduction of Ce in BT, changing our existing understanding of its behavior.[21,25–29] While other lanthanides and transition metals can also induce magnetism in BT, they often require higher concentrations that may compromise its ferroelectric properties. Although many studies have discussed ferromagnetism in BT with transition metal doping, few have focused on the impact of cerium doping specifically at the Ba^{2+} (A) site. Considering this gap, it is worth investigating how this A-site substitution of Ce impacts BT ceramics.

This study focuses on the synthesis of A-site-substituted $Ba_{1-x}Ce_xTiO_3$ (x = 0, 0.5, 1, and 1.5%) ceramics using a sol–gel chemical synthesis technique. Sol–gel processing provides a distinctive advantage by facilitating the synthesis of ceramics at lower temperatures, thereby significantly influencing their structural and electrical characteristics. The structural information of the prepared ceramics was obtained through Rietveld refinement of the X-ray diffraction (XRD) data, and the morphology was studied using field emission scanning electron microscopy (FESEM). Raman spectroscopy was used to obtain information related to the chemical composition. Furthermore, vibrating sample magnetometry (VSM) was utilized for the DC

magnetic response of the samples, whereas impedance analysis was used to determine the effect of the dopant on the dielectric properties. Through systematic exploration, this study examines the structural, dielectric, and magnetic properties inherent in BT and BCT ceramics. The presented findings contribute to a nuanced understanding of the intricate interplay between Ce substitution, sol–gel processing parameters, and the resulting material characteristics. This work not only expands the fundamental knowledge of the studied system, but also holds potential implications for advancing functional materials with tailored properties, thereby creating opportunities for applications in diverse technological domains.

2. Synthesis and characterization

The sol–gel method was adopted for the synthesis of BT and BCT ceramics. A solution was prepared by dissolving different mol% of cerium(III) acetate in 25 ml of 2-ethyl hexanoic acid and mixed with the desired amount of barium acetate and tetra-*n*-butyl orthotitanate with continuous stirring. The resulting mixture was heated at 150 °C until it completely dried. The dried specimen was then crushed into a fine powder, and the powder samples were annealed at 1300 °C for 5 hours in a furnace. To perform the electrical measurements, pellets of the synthesized ceramic powder were prepared by compressing sintered powders in a die with a diameter of 10 mm under a pressure of 3.5 tons for half an hour at room temperature, using polyvinyl alcohol as a binding agent. The BCT pellets were then sintered at 1350 °C for 30 min. The prepared ceramics were examined by various experimental methods. A comprehensive characterization approach was undertaken to elucidate the structural, compositional, and functional properties of the fabricated BT and BCT ceramics. XRD analysis using an X'Pert PRO diffractometer with Cu K_α radiation (λ = 1.54 Å) was employed to identify the crystal phases present in the samples. This assessment ensured the formation of the desired crystalline phases and unveiled any potentially detrimental secondary phases that might compromise the material performance. Further insights into the local atomic order and subtle structural variations were obtained through Raman spectroscopy using a LabRAM HR Evolution (Horiba, Japan) with a 532 nm excitation laser. This technique provides valuable information regarding the chemical composition and bonding characteristics of the ceramics. The microstructural features, including grain size, morphology, and the presence of defects or porosity, were investigated using field emission scanning electron microscopy (FESEM) on a Nova NanoSEM 450 (USA). A thorough understanding of the microstructure is crucial because it directly influences the mechanical and functional properties of the final material. In addition, the magnetic properties of the ceramics were determined using a MicroSense EV7 system (USA). These data are particularly relevant for applications where magnetic behavior plays a significant role. Finally, the dielectric properties, such as the dielectric constant and loss tangent, were assessed using a Wayne Kerr 6500 B impedance analyzer. This information sheds light on the interaction of the material with electric fields, a key factor for applications involving electrical insulation or energy storage.

3. Results and discussion

Fig. 1 displays the XRD patterns of BT and BCT ceramics post-annealed at 1300 °C. The scan covers the entire 2θ range from 20° to 70° conducted at a speed of 0.02° per second for all the samples. Notably, each sample exhibited well-defined sharp reflection lines, indicating a high degree of crystallization.[30] In the XRD data of all BCT ceramics with Ce substitution up to 1.5 mol%, pristine perovskite structure growth is evident, devoid of any discernible impurities. This underscores the successful substitution of Ce^{3+} ions into the BT lattice. However, a further increase in the Ce content to 2 mol% resulted in the emergence of impurities, as corroborated by the XRD patterns shown in Fig. 1. Consequently, subsequent characterizations were confined to the BCT samples up to x = 1.5%. The diffraction

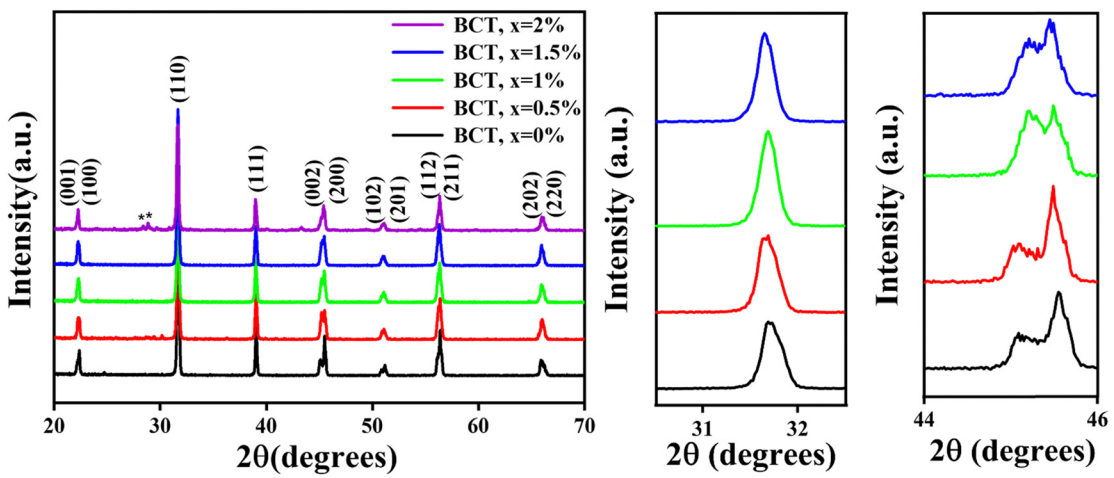

Fig. 1 XRD patterns of BT and BCT ceramics with x = 0.5%, 1%, 1.5% and 2% (left); shift of the peaks at 31° (center) and 45° (right) on cerium doping.

peaks align with the standard patterns of the tetragonal phase of BT (ICSD card 01-075-2117), with dual (002)/(200) peaks at $\sim 2\theta = 45^\circ$, confirming the tetragonal structure formation in these samples.[31] The most intense peak, denoted as (110), manifested prominently near $2\theta \approx 31^\circ$ in the XRD spectra. Further validation of the tetragonal structural evolution in these samples was affirmed by the discernible splitting of additional peaks at $2\theta \approx 53^\circ$, 57°, and 65°. A subtle shift of peaks (*e.g.*, at 45°) towards higher 2θ values is observed with increasing Ce content in BT ceramics, as anticipated due to the comparatively smaller ionic radius of Ce^{3+} ions (1.07 Å) relative to Ba^{2+} ions (1.35 Å). The crystallite size was determined using the Scherrer formula:[32]

$$d = \frac{0.9\lambda}{\beta_{hkl} \cos \theta} \quad (1)$$

where λ = 1.5406 Å is the wavelength of the X-ray (Cu K_α), β_{hkl} is the full width at half maximum, and θ is Bragg's angle. The resulting crystallite sizes for the BCT ceramics are summarized in Table 1, revealing an increase in the crystallite size with increasing Ce content. This phenomenon is indicative of an augmented unit cell volume and a reduced tetragonal *c*/*a* ratio, excluding the sample with 1 mol% Ce substitution. The Williamson–Hall (W–H) method addresses both instrumental and strain broadening enabling us to calculate the strain induced in the lattice.[33] The W–H plots for BT and BCT samples are shown in Fig. S1 (ESI†). The negative slope found for all the samples in the W–H plots indicates that there is a tensile strain induced in each of these samples. Moreover, the strain values decreased with increasing dopant concentration, suggesting that Ce ions are efficiently incorporated in the BT lattice. The introduction of Ce^{3+} ions, which are smaller than Ba^{2+} ions, at the Ba^{2+} site induces oxygen vacancies, potentially extending the Ti site substitution. Such substitutions generally result in lattice strain elevation, which primarily contributes to the increased crystallite size.[34] Consistent with prior research by Kumar *et al.*,[15] a direct correlation was established between the increase in the Ce dopant concentration and the likelihood of oxygen vacancy formation. The atypical structural response observed in BCT with 1 mol% Ce content is postulated to stem from lattice strain saturation due to the transition from substitution site A to B. Furthermore, Rietveld refinement of the powder XRD spectra of BT and BCT ceramics was carried out using FullProf software. The pseudo-Voigt function, represented as the summation of Gaussian and Lorentzian functions, was employed as the peak profile function.[35] The scale factor, background, isothermal parameters, occupancy, and instrumental

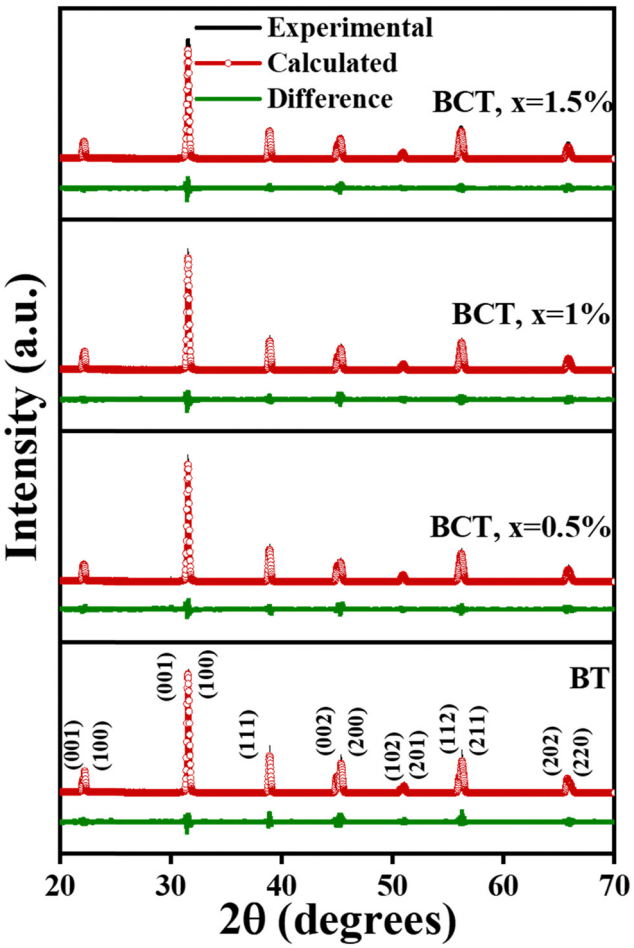

Fig. 2 Rietveld refined XRD patterns of BT and BCT ceramics.

broadening were refined to achieve a fitting congruent with the anticipated structural model. The chi-square (χ^2) values resulting from the Rietveld fitting were close to unity, signifying a fitting adequacy for the X-ray diffraction of BCT ceramics.[36,37] Fig. 2 shows the Rietveld refined powder XRD profiles of BT and BCT ceramics, facilitating a comprehensive structural analysis of the specimens. The various structural parameters obtained from Rietveld fitting are listed in Table 2. Fig. 3 displays the crystal lattice created with Vesta using the improved parameters obtained after refinement.

The microstructural properties of the BCT ceramics were investigated using FESEM. Fig. 4 shows the FESEM micrographs and histograms illustrating the grain size distribution of the BCT ceramics. From the fitting of histograms to the normal distribution function given below, it is possible to

Table 1 Variation in the crystalline size, unit cell volume, and tetragonality *c*/*a* ratio of BCT ceramics

	Lattice parameters					
Ce concentration (mol%)	*a* (Å)	*c* (Å)	Crystallite size (nm)	Unit cell volume (Å^3)	Tetragonality (*c*/*a*)	Grain size (nm)
0	3.9979	4.0309	34.399	64.4254	1.00843	738.4
0.5	4.0021	4.0259	38.837	64.4827	1.00595	826.6
1	4.0009	4.0260	38.658	64.4286	1.00602	815.4
1.5	4.0035	4.0256	38.901	64.5214	1.00552	899.3

Table 2 Rietveld refinement parameters of BCT ceramics with varying Ce concentrations

Ce concentration (mol%)	χ^2	Bragg factor	R_f	R_p	R_{wp}	R_{exp}
0	1.22	5.870	5.335	26.2	31.8	28.78
0.5	1.51	6.358	4.559	22.0	29.9	24.35
1	1.13	5.653	5.585	25.1	30.6	28.81
1.5	1.06	4.157	3.308	18.2	25.8	25.10

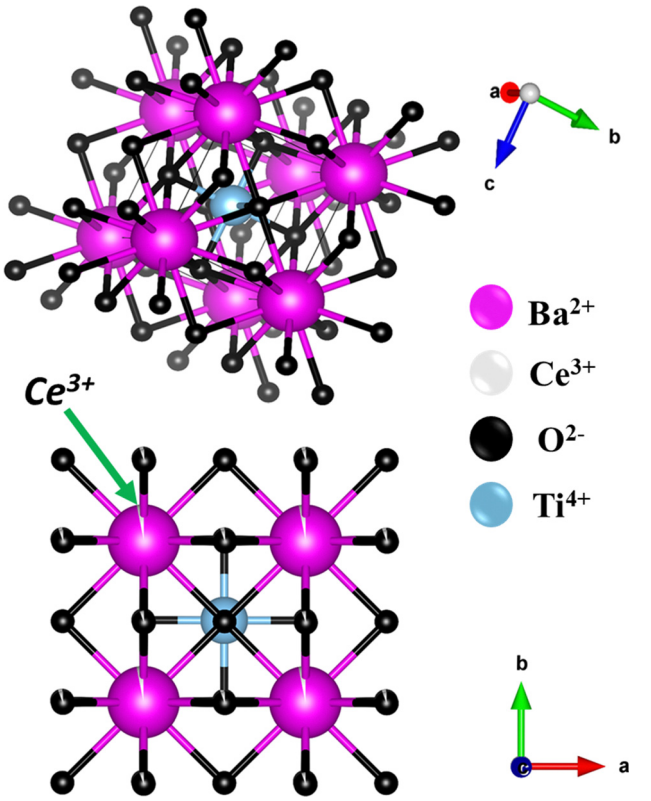

Fig. 3 Crystal structures of BT and BCT ceramics generated using Vesta software using Rietveld refined structural parameters.

determine the average grain size of BCT ceramics:[38,39]

$$f(x) = \frac{1}{\sigma\sqrt{2\pi}}\exp\left(\frac{-(x-\mu)^2}{2\sigma^2}\right) \quad (2)$$

where x represents the average grain size, σ represents the standard deviation of x, and μ is the mean of x. All the BCT ceramics exhibited well-defined microstructural characteristics. The measured grain sizes of the prepared samples are shown in Table 2. It has been observed that, with Ce substitution, the overall grain size of BT increases, which is attributed to the substitution of Ce^{3+} and Ce^{4+} at the A- and B-sites, respectively.[27] The presence of polymorphic coarse and small grains is evident in the micrographs. It is also observed from the FESEM images that the ceramic becomes denser with Ce substitution, and microstructural evolution exhibits relatively larger grains with well-defined grain boundaries. The observed average grain size values are 738.4, 826.6, 815.4, and 899.3 nm for BT, BCT (x = 0.5), BCT (x = 1) and BCT (x = 1.5) ceramics, respectively. However, the slightly decreasing trend of the grain size observed for the 1% Ce-substituted BT ceramic could be explained by the development of fewer vacant oxygen spots in this particular specimen. The generation of oxygen vacancies in BCT ceramics was also confirmed by Senthil *et al.*[40] using XPS analysis.

To gain more insights into the structural changes in BT ceramics with Ce content, the Raman study was performed on the prepared samples. The Raman spectra of BT and BCT ceramics spanning the wavenumber region from 0 to 1200 cm^{-1} were measured by exciting the samples with monochromatic light of wavelength $\lambda \approx 532$ nm (Fig. 5).[41,42] It is widely known that, above the Curie temperature, BT is in a paraelectric phase with cubic symmetry, which results in it being Raman inactive, while ferroelectric symmetry makes it Raman active. BT has 12 optical modes according to the formula $(3N - 3)$, N being the number of atoms per unit cell.[43] For tetragonal BT, there are A1, B1, and E modes. Because of the long-range electrostatic interactions among Ti and O in Ti–O_6 octahedra, there appears a splitting of A1 and E modes into longitudinal optical (LO) and transverse optical (TO) modes.[42] The Raman spectra of the BCT ceramics displayed distinct optical modes at 180 cm^{-1}, 263 cm^{-1}, 305 cm^{-1}, 514 cm^{-1} and 715 cm^{-1}, analogous to the tetragonal phase of BT.[44] A band with a dip was observed at 180 cm^{-1} owing to the anharmonic interaction of three A1 (TO) phonon modes.[43,44] The optical mode at 264 cm^{-1} is designated as the A1 (TO) phonon mode. The optical modes observed at 305 cm^{-1} and 715 cm^{-1} being the most prominent confirmed the tetragonal structure. These optical modes are associated with the [B1, E (TO + LO)] and [A1 (LO), E (LO)] phonon modes. In addition, a broadband with a phonon mode [E (TO), A1 (TO)] at 514 cm^{-1} was obtained, attributed to the interaction of structural defects or Ti^{4+} disorder with normal phonons.[45] The tetragonal structure remains intact even in BCT with x = 1.5 mol%, as is evident from the presence of optical modes around 305 cm^{-1} and 715 cm^{-1}. Thus, it is concluded that there is no structural transformation in BCT ceramics, even at higher cerium concentrations, as validated through XRD and Raman analysis. However, as the concentration of Ce dopant increased, the strength of the optical modes weakened and broadened. Furthermore, a blue shift (from 715 cm^{-1} to 717 cm^{-1}) in the Raman peak at 715 cm^{-1} was also visible with an increase in Ce doping.

In bulk, BT is diamagnetic, and to induce the magnetic properties for the multiferroic and magnetoelectric applications while maintaining its high dielectric and ferroelectric properties, Ce^{3+} is introduced in the crystal lattice. Fig. 6 shows the ferromagnetic properties of the BCT samples after subtracting the diamagnetic contribution. The magnetization *vs.* magnetic field (M–H) curves for BCT ceramics under an applied field of 20 kOe are shown in Fig. 6(b)–(d); however, for the BT sample (Fig. 6(a)), it saturates at a much lower applied magnetic field of approximately 1500 Oe.[39] BCT ceramics show ferromagnetic characteristics at a lower applied magnetic

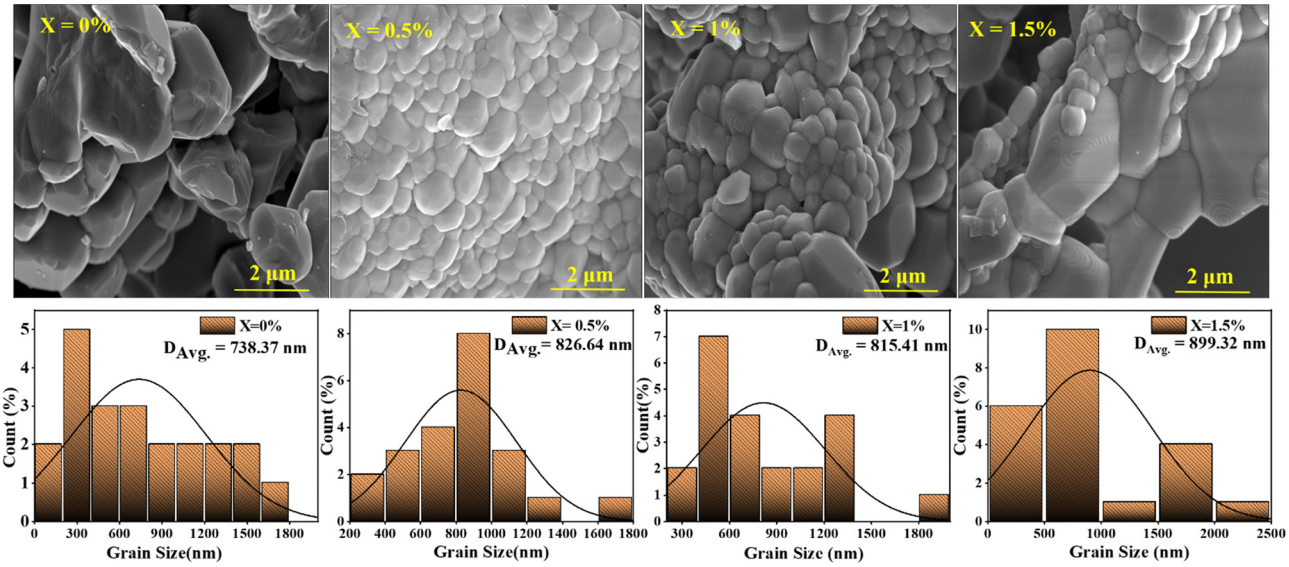

Fig. 4 FESEM images of BT and BCT ceramics annealed at 1300 °C along with their histograms of grain size distribution fitted to eqn (2).

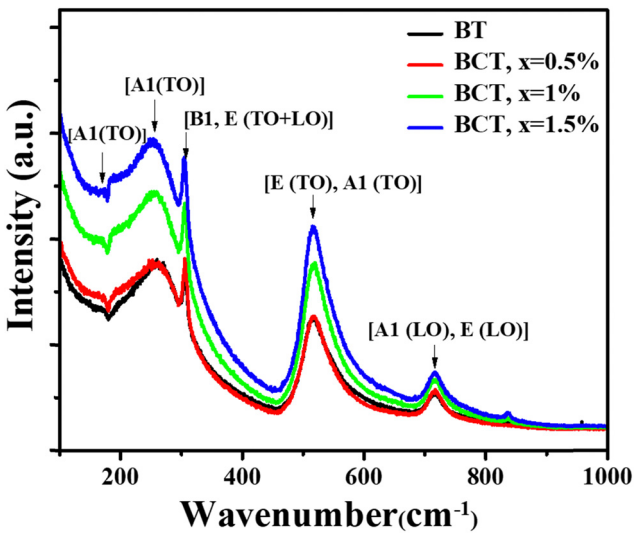

Fig. 5 Raman spectra of BT and BCT ceramics with varying Ce concentrations.

field and display diamagnetic characteristics at a higher field. The existence of numerous ionic states of Ce atoms may help to explain this magnetization behavior. After subtracting the diamagnetic response, the presence of ferromagnetic and paramagnetic contributions in the BCT ceramics results in *M*–*H* curves, as shown in Fig. 6(a)–(d).[46] The fitting of the *M*–*H* curves was performed by considering the ferromagnetic and paramagnetic contributions according to the following equation:[47–49]

$$M(H) = \frac{2M_s}{\pi}\tan^{-1}\left[\frac{H \pm H_c}{H_c}\tan\left(\frac{\pi S}{2}\right)\right] + \chi \cdot H \qquad (3)$$

The ferromagnetic contribution fits according to the above equation, where the BCT ceramics are magnetized under the applied field. In the above equation, the 1st term describes the ferromagnetic contribution, and the 2nd term describes the paramagnetic contribution in BCT ceramics, where M_s, H_c, $S = \frac{M_r}{M_s}$, and χ are the saturation magnetization, coercive field, squareness ratio, and magnetic susceptibility, respectively.[47–51] In our results, the value of χ is significantly less than 1, and therefore the diamagnetic behavior can be observed at higher fields. In addition, the insets in Fig. 6(a)–(d) at the bottom right corner are the magnified snapshots of the *M*–*H* curves near the origin, where the experimental data points and the fitting curves signify good agreement with the equation and the optimized theoretical parameters such as M_s (th), H_c (th), and M_r (th) are shown in Table 3.

The observed *M*–*H* curves of the BCT samples (at Ce concentrations of 0.5%, 1%, and 1.5%) show weak ferromagnetism; however, it was found to be stronger than that observed in BT since BT is diamagnetic in bulk and becomes ferromagnetic under certain conditions, such as vacancy induction, the impact of the Ba/Ti ratio, edge dislocations, and defects at nanoscale sizes of BT particles.[43,44] Additionally, numerous studies have reported a slight magnetic influence in its bulk form, which exactly matches the present findings for BT samples.[52–55] Among all the samples, the BCT (x = 0.5%) exhibited the highest magnetization value of $M_s \approx 3.41 \times 10^{-3}$ emu g^{-1} with a coercive field value (H_c) of ~58.96 Oe. The M_s values of the BCT ceramics demonstrate an upward trend with an increase in Ce content up to 0.5 mol%; a similar trend was reported at 1 mol%.[39] On further increasing the Ce concentration to 1 and 1.5 mol%, a decrease in M_s (Fig. 6(b)) can be observed, while there is a gradual increase in H_c (Table 3). In addition, the magnetocrystalline anisotropy energy

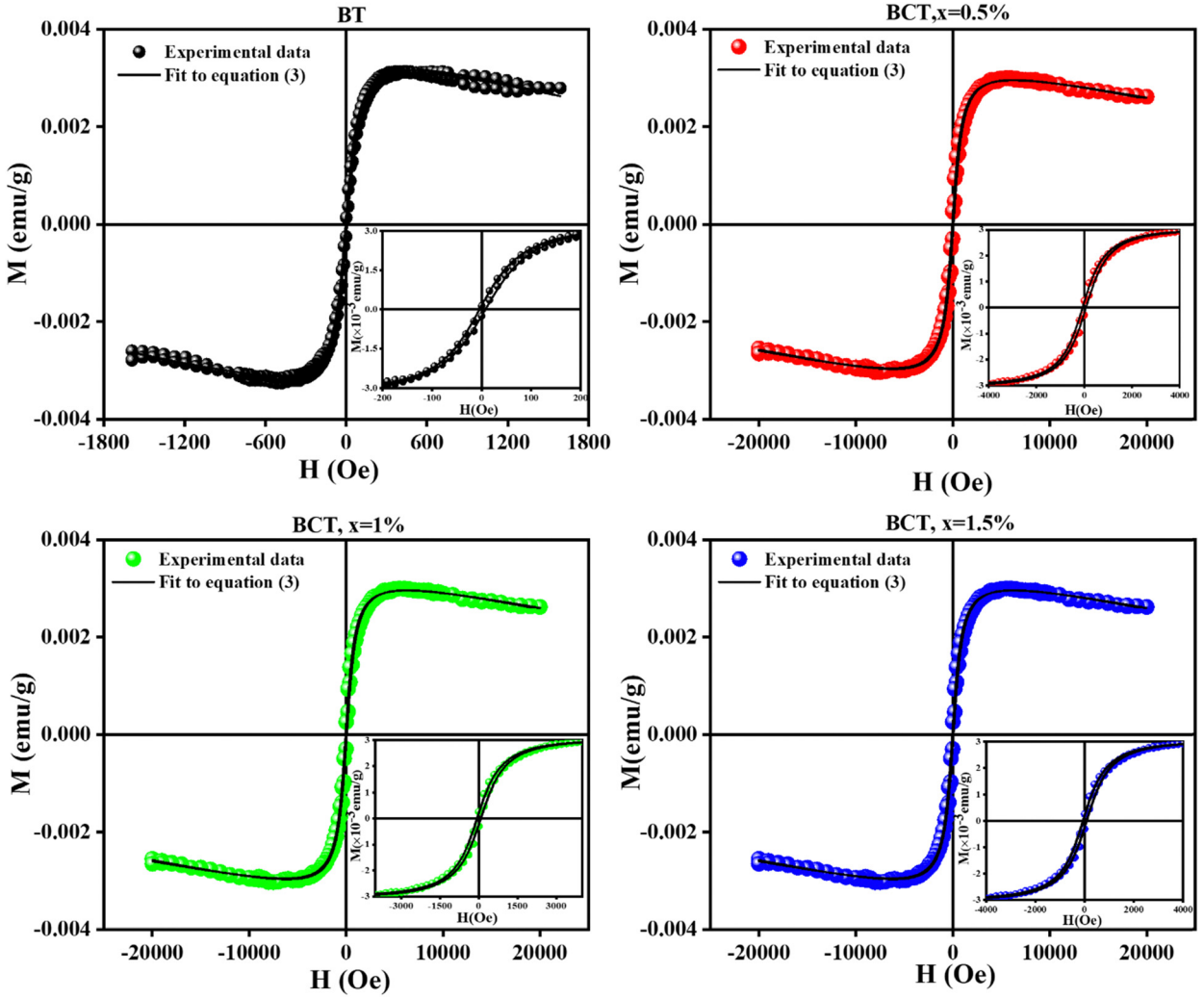

Fig. 6 *M*–*H* curves of (a) BT and (b)–(d) BCT ceramics (0.5, 1, and 1.5 mol%) at room temperature. The insets at the right bottom corner show the magnified snapshots near the origin. The black solid line overlapping the data points represents the fitting of the *M*–*H* loop by using eqn (3).

Table 3 Saturation magnetization (M_s) and coercive field (H_c) values of BCT ceramics

Concentration (in mol%)	M_s (exp) (emu g^{-1})	H_c (exp) (Oe)	M_r (exp) (emu g^{-1})	M_s (th) (in emu g^{-1}) $M = \frac{2M_s}{\pi}\tan^{-1}\left[\frac{H+H_c}{H_c}\tan\left(\frac{\pi S}{2}\right)+\chi H\right]$	H_c (th) (Oe)	M_r (th) (emu g^{-1})	M_s (th) (LAS fit) (emu g^{-1}) $M = M_s\left[1-\frac{b}{H^2}\right]+\chi H$	$K = \frac{M_s H_c}{2}\times 10^{-4}$ (erg cm^{-3})
0	3.14×10^{-3}	3.70	1.38×10^{-4}	3.74×10^{-3}	4.492	1.60×10^{-4}	3.45×10^{-3}	32.41
0.5	3.41×10^{-3}	58.96	1.84×10^{-4}	4.05×10^{-3}	48.607	1.77×10^{-4}	3.75×10^{-3}	597.47
1	3×10^{-3}	68.11	2.60×10^{-4}	3.43×10^{-3}	68.203	2.12×10^{-4}	3.28×10^{-3}	597.69
1.5	1.76×10^{-3}	71.39	1.68×10^{-4}	2.06×10^{-3}	70.251	1.92×10^{-4}	1.91×10^{-3}	277.31

(MCA) of BCT ceramics can be defined as $\left(K = \frac{M_s H_c}{2}\right)$ where M_s and H_c are inversely dependent to each other justifying the observed trend of coercivity of BCT ceramics.[49,56,57]

The enhancement in magnetization may be due to the interaction of the unpaired electrons of $4f^1$ (Ce^{3+}) with vacancies present in the material and because of the redistribution or sharing of energy caused by the hybridization between the electrons of $4f^1$ (Ce^{3+}) with $5d^0$ (Ce^{3+}), $6s^0$ (Ce^{3+}), and the electrons of the 2p subshell of O^{2-}.[58] In addition to these factors, the hybridization of the electrons of Ce^{4+} ions with the $4f^0$, $5d^0$, and $6s^0$ subshells of Ce^{4+} ions and the electrons of the 2p subshells of O^{2-} also contributes to magnetization.[59] These Ce^{4+} ions originate from Ce^{3+} ions, which provide oxygen

vacancies to make conversion possible.[59] At higher Ce concentrations, there is a decrease in magnetization, which may be attributed to the diamagnetic contribution. Mohanapriya *et al.*[60] reported that, at higher concentrations of Ce substitution in BT, numerous localized 4f electrons occur, which contribute to the diamagnetic characteristic and hence the decrease in the magnetization. In addition, first-principles studies also suggest that the origin of ferromagnetism in non-magnetic ferroelectric BT is the oxygen and titanium vacancies in the crystal lattices.[55] Several theoretical studies have also found that BT nanoparticles have a small amount of ferromagnetism, which is supported by spin-density functional theory.[55,61] With the substitution of a suitable dopant, magnetism can be induced in bulk BT ceramics.[46,48,62,63] Here, in BT ceramics, it has been found that magnetism increases gradually with Ce doping. In this work, maximum substitution up to 1.5 mol% was performed without hampering the perovskite structure on the Ba site because Ba^{2+} ions are replaced by Ce^{3+} ions in the nearest neighboring sites, which results in the induction of ferromagnetism in BT ceramics. As revealed by experimental and theoretical investigations, the ferromagnetism of BT is caused by titanium and oxygen vacancies.[61,64] Thus, in our results Ce^{3+} ions replaced Ba^{2+}, whereas some Ce^{4+} ions were substituted at Ti^{4+} sites because the actual substitution depends generally on the Ba/Ti ratio.[42] It is worth noting that M_s values are relatively low. While these values may seem modest compared to some other materials, the unique combination of properties such as ferroelectricity, dielectric properties and weak ferromagnetism in BCT ceramics offers significant advantages in various applications such as spintronics, energy harvesting, data storage, *etc.*[65–68]

Fig. 7(a) shows the frequency response of the dielectric constant behavior of the BCT ceramics measured at room temperature. The dielectric responses of these samples were examined at frequencies ranging from 1 kHz to 1 MHz. All samples had dielectric constant values that were slightly higher for low-frequency values and become progressively lower as the frequency increases.[69] It can be seen from Fig. 7 that the dielectric constant behavior becomes almost dispersion-less beyond a 1.5 kHz frequency.[27,70]

The dielectric response can be understood in terms of the different types of polarizations present in the samples, which include atomic, dipolar, electronic, space charge, and interfacial polarizations. The grain boundaries in dielectric materials are highly restrictive; therefore, upon exposing the material to an external electric field, the charges present on the surface are assembled near the boundaries or interface between the grains. This results in the generation of interfacial polarization within the sample. Interfacial polarization and space charge polarization are responsible for the higher dielectric constant values at lower frequencies, but interfacial polarization fails to respond at higher frequencies. Thus, for higher-frequency values (rapidly varying electric fields), some dipoles are unable to imitate this variation in the electric field. At higher frequencies, the decreased value of the dielectric constant can be attributed mainly to the contribution of electronic and atomic

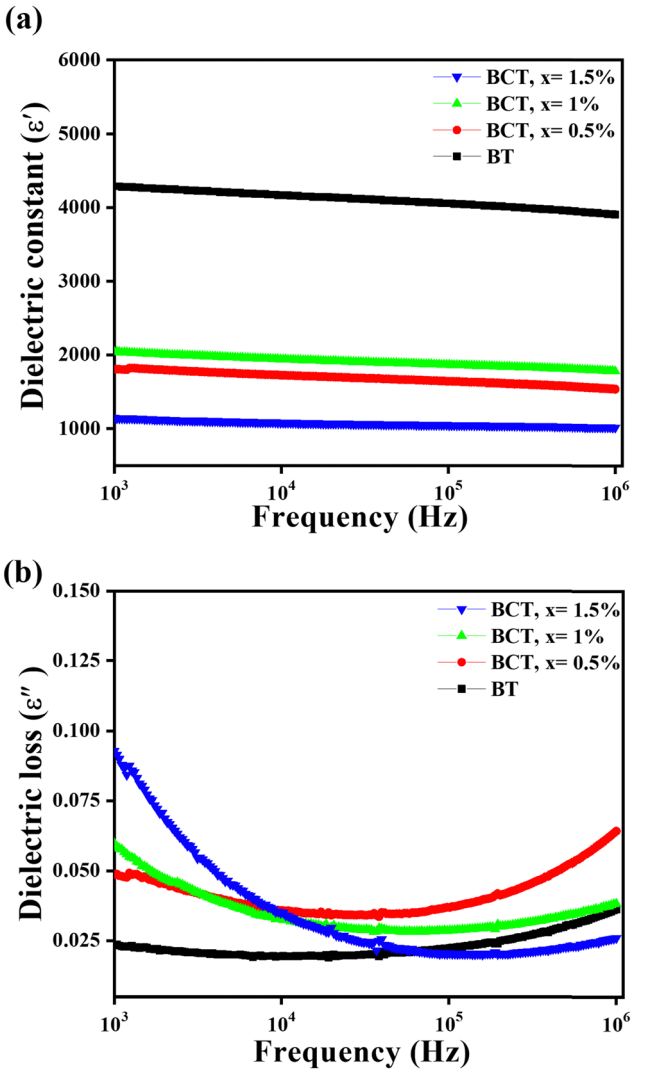

Fig. 7 Variation of the (a) dielectric constant and (b) dielectric loss of BT and BCT ceramics with varying frequencies.

polarization.[27] Thus, the contribution due to the interfacial polarization is not large compared to the lower frequency values, which causes decreased values of the dielectric constant. This effect was originally proposed by Koop, where the effect of voltage drop throughout the grain boundaries remained larger at low frequencies.[71] The dielectric constant decreased at higher frequencies because the contributions from space charge polarization decreased, as explained by the Maxwell–Wagner mechanism.[72,73]

Overall, the dielectric constant decreases with increasing Ce substitution content. This behavior can be understood in terms of the decrease in the tetragonality of samples with increasing Ce concentration. This dielectric behavior is consistent with the reported work, which elucidates the decrease in the dielectric constant with a tetragonality factor.[62,70–72] The tetragonality factor decreases with increasing Ce content because of additional oxygen vacancies within the lattice. This, in turn, leads to a further reduction in the dielectric constant. It can be clearly

seen that the tetragonality factor significantly influences the dielectric constant values. A similar behavior of the dielectric constant was reported by Choudhary *et al.*[74] and Sarah *et al.*[75] The dielectric loss behavior of various samples as a function of frequency at room temperature is shown in Fig. 7(b).

The loss tangent or loss factor ($\tan\delta$) represents the energy dissipated in the dielectric material during polarization. As shown in Fig. 7(b), the dielectric loss initially decreases with increasing frequency, saturates, and then slightly increases at higher frequencies. The increase in the dielectric loss at higher frequencies is attributed to the resonance effect of the electrical leads employed in the measurement unit. The variations in the dielectric constant and dielectric loss values with dopant concentration at a frequency of 1 kHz for the BCT ceramics are listed in Table 4. One can see an increase in the dielectric loss factor of the BCT ceramics with Ce substitution. This trend can be understood in terms of the increased number of vacant oxygen sites in the samples with an increase in the doping concentration. It is well known that a lower value of dielectric constant leads to a higher resonant frequency. Therefore, BCT ceramics with decreasing dielectric constants can be advantageous for applications such as microwave and millimeter-wave devices, enabling the design of smaller and more compact dielectric resonators. While an increase in the dielectric losses is also observed, the maximum value remains relatively low at 0.093. This favorable characteristic is essential for applications where minimizing energy dissipation is crucial.

Fig. 8 illustrates the frequency-dependent behavior of the real and imaginary AC conductivity parts of all BCT ceramics at RT. All samples exhibited an increase in AC conductivity with increasing frequency, a common characteristic of dielectric materials attributed to enhanced charge carrier mobility at higher frequencies.[76] The plots showed a linear relationship with frequency across a wide range, deviating only at low frequencies. Such behavior suggests a hopping process in which charge carriers transition between localized states.[77,78] Enhanced conductivity results from the efficient hopping of charge carriers at higher applied field frequencies. Meanwhile, pure BT had lower conductivity than doped counterparts suggesting that Ce doping may have introduced additional charge carriers or pathways for conduction. Notably, the sample with the highest doping concentration had the highest conductivity at lower frequencies. However, at higher frequencies, the trend reversed, leaving a less apparent link between conductivity and dopant concentration. In contrast, the imaginary component of conductivity constantly declined as Ce doping increased, with

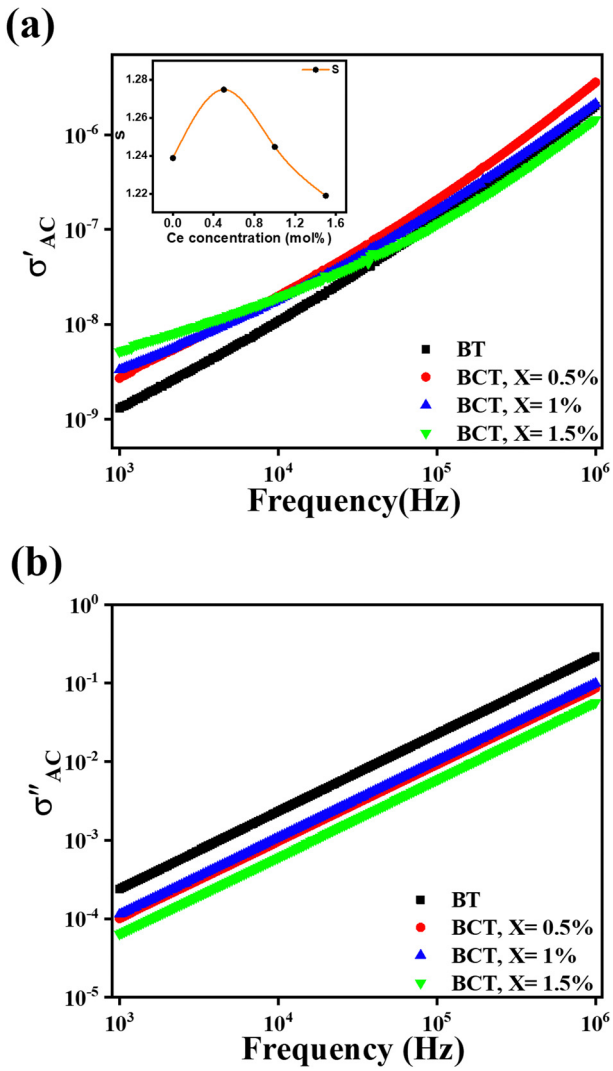

Fig. 8 Variation of (a) the real part of AC conductivity (the inset image shows the variation of the frequency exponent *s* with Ce concentration) and (b) the imaginary part of AC conductivity of BCT ceramics against frequency.

Table 4 Room-temperature dielectric constant and dielectric loss values of BCT ceramics measured at 1 kHz

Ce concentration (mol%)	Tetragonality (c/a)	Dielectric constant (ε')	Dielectric loss (at 1 kHz)
0	1.00823	4288	0.023
0.5	1.00595	1806	0.049
1	1.00602	2043	0.059
1.5	1.00552	1148	0.093

the exception of BCT x = 1%, which showed an odd increase. Conductivity spectra (Fig. 8(a)) were then well fitted to Jonscher's law given by eqn (4):[79]

$$\sigma_{AC} = \sigma_t - \sigma_{DC} = A\omega^s \quad (4)$$

where σ_{DC} represents the frequency-independent DC conductivity (the limiting value of total conductivity (σ_t) as the frequency approaches zero). The fits yielded the power law exponent (s) that represents the extent of interaction between mobile ions. All BCT samples had s values greater than one, indicating a frequency-dependent increase in dielectric loss (Table 5). The inset image in the real conductivity *vs.* frequency plot shows how Ce concentration affects the value of s.

To perform a better investigation of the relaxation dynamics, the complex dielectric modulus (M^*) was calculated using

Table 5 Values of s and the figure of merit for different BCT samples

Ce concentration (mol%)	s	Figure of merit (F)
0	1.2388	5.17×10^{-10}
0.5	1.2749	23×10^{-10}
1	1.2447	12×10^{-10}
1.5	1.2189	14×10^{-10}

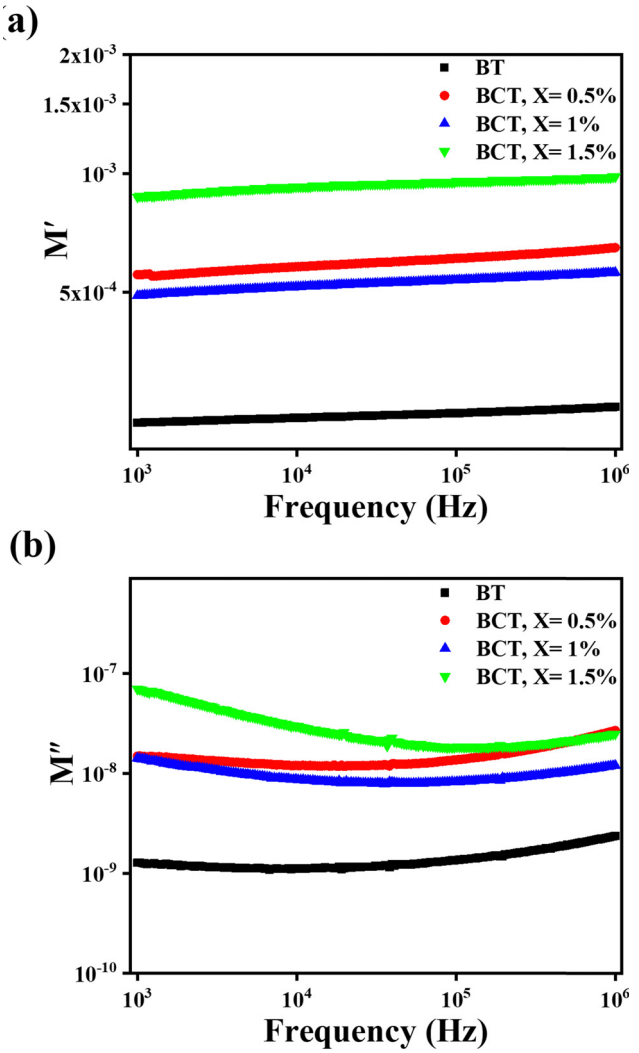

Fig. 9 Variation of the (a) real component of the dielectric modulus (M') and (b) imaginary component of the dielectric modulus (M'') with frequency.

eqn (5) and its variation with frequency is displayed (Fig. 9) as it suppresses the contributions due to the electrode polarization to give a more direct view of the relaxation time distribution.[80,81]

$$M^* = \frac{1}{\varepsilon^*} \quad (5)$$

$$M' = \frac{\varepsilon'_r}{\varepsilon'^2_r + \varepsilon''^2_r} \quad (6)$$

$$M' = \frac{\varepsilon'_r}{\varepsilon'^2_r + \varepsilon''^2_r} \quad (7)$$

As shown in Fig. 9, the real component (M') of the dielectric modulus exhibited a general upward trend with increasing content of Ce. However, the 1% Ce sample deviated from this pattern, possibly because some Ce ions occupied the B-site, resulting in an increase in the dielectric constant (as observed in Fig. 7) and hence a higher M'. The observed pattern implies that the energy storage capacity decreases as the Ce concentration and frequency increase. This could be due to the inability of dipoles to keep up with rapidly changing electric fields, paired with the introduction of defects or voids produced by Ce doping. These faults can increase conductivity, which reduces the ability of the material to store electrical energy. Similar findings were observed for the imaginary component of the dielectric modulus (M''). The absence of peaks in the M'' *versus* frequency plots indicates that there are no relaxation processes in the frequency range being studied.[82,83] Additionally, the figure of merit (F), calculated as the ratio of AC conductivity to the dielectric constant, was determined to assess the potential of these ceramics for solar cell applications. A higher F value generally indicates improved suitability for such applications and it can be seen from Table 4 that there is an increase in the value of F on doping it with Ce.

4. Conclusion

Cerium-doped $BaTiO_3$ ceramics, with the composition $Ba_{1-x}Ce_xTiO_3$ ($0\% \leq x \leq 1.5\%$), were synthesized using a sol–gel method. No secondary phase formation occurs up to 1.5 mol% Ce substitution, which confirms the complete dissolution of Ce atoms in the BT solid solution at the applied sintering temperature. XRD analysis revealed no structural transformation in any of the BCT ceramics. In addition, the volume of the unit cell and crystallite size of the samples increased, possibly linked to the increase in vacancies. The FESEM images showed dense grain growth, with the grain size expanding proportionally to the Ce concentration. The Raman spectra support the XRD analysis results, and the Raman mode at 715 cm^{-1} undergoes a blue shift from 715 cm^{-1} to 717 cm^{-1} with increasing Ce content. The induction of magnetism was observed in the BCT samples, and the highest M_s value was obtained at 0.5% doping; however, further doping decreased the M_s values. This decrease in the M_s values can be attributed to the electrons of the 4f-subshell furnishing diamagnetic contributions to BCT ceramics with 1% and 1.5% Ce. Concurrently, an increase in the H_c values was also observed, likely correlated with the magnetocrystalline anisotropy. The presence of spin charge density and generated oxygen vacancies are considered to be the cause of ferromagnetism in BCT ceramics. This suggests their potential as magnetoelectric multiferroic materials for applications in fields like spintronics, data storage, and haptic devices, with the possibility of further improvements. Further electrical properties were obtained using dielectric

measurement indicating the AC conductivity increased with frequency due to enhanced carrier mobility. Additionally, Ce doping led to higher AC conductivity, suggesting the introduction of additional charge carriers or conduction pathways. A decrease in dielectric constant values is observed with a slight increase for 1% Ce doping, which is consistent with the *c*/*a* ratio. A reduction in the dielectric constant made these ceramics suitable for high resonant frequency applications like millimeter- and micro-wave devices. While dielectric loss increased with Ce doping, it remained well below 0.1, making these materials ideal for applications requiring minimum energy losses. To further enhance the magnetic and magnetoelectric properties of these multifunctional materials, exploring the effects of incorporating the layers of ferromagnetic materials and employing additional co-dopants like Fe, Ni and Co in conjunction with Ce is recommended.

Author contributions

Rahul Sharma: conceptualization, methodology, investigation, data analysis, writing – original draft. Shreya Sinha: investigation, data analysis, writing – review & editing. Rahul Singh: data analysis, investigation, writing – review & editing. Saurabh Pathak: data analysis, validation, supervision, writing – review & editing. Barsha Borgohain: writing – review & editing. Noorjahan: supervision, writing – review & editing. NS Negi: conceptualization, resources, writing – review & editing, supervision.

Data availability

The raw data supporting the findings of this study are available from the corresponding author upon request.

Conflicts of interest

The authors declare that they have no known competing financial interests or personal relationships that could have appeared to influence the work reported in this paper.

Acknowledgements

The authors would like to thank Professor N. S. Negi for the guidance throughout the completion of the research work, financial support and for providing the lab facilities at the Department of Physics, Himachal Pradesh University Shimla. The authors acknowledge the financial support provided by the Central University of Himachal Pradesh & University Grants Commission, India. Dr S. P. acknowledges Seoul National University's Materials Education/Research Division for Creative Global Leaders for the support.

References

1 R. Nandan, R. Syal, S. Kumar and N. S. Negi, Enhanced room-temperature electrocaloric and pyroelectric responses around morphotropic phase boundary and energy storage performance of lead-free $Ba_{0.85}Ca_{0.15}Hf_{0.10}Ti_{0.90}O_3$ ceramics sintered at various temperatures, *J. Alloys Compd.*, 2023, **968**, 171856, DOI: 10.1016/j.jallcom.2023.171856.

2 J. Wang, Z. Xin, Y. Wang, H. Hao, S. Liu, Q. Wang and J. Zhai, Reinforced energy storage performance of poly(vinylidene fluoride) composite films by filling with surface fluorinated one-dimensional barium titanate nanofibers, *J. Alloys Compd.*, 2023, **966**, 171601, DOI: 10.1016/j.jallcom.2023.171601.

3 T. Zhao, Y. Ye, K. Guo, R. Cui, M. Zhang, X. Wang, B. Zhang, J. Zhang and C. Deng, High energy storage properties of calcium-doped barium titanate thin films with high breakdown field strength, *J. Alloys Compd.*, 2024, **970**, 172487, DOI: 10.1016/j.jallcom.2023.172487.

4 C.-C. Hsu, W.-C. Wu, W.-C. Jhang, Z.-K. Xiao, H.-C. Chang, M.-Y. Hsu and U. Nanda, Barium titanate write-once read-many times resistive memory with an ultra-high on/off current ratio of 108, *J. Alloys Compd.*, 2024, **988**, 174252, DOI: 10.1016/j.jallcom.2024.174252.

5 R. Bujakiewicz-Koronska, Ł. Gondek, L. Vasylechko, M. Balanda, E. Juszynska-Galazka, M. Galazka, D. Majda, W. Piekarczyk, A. Zywczak, A. Cizman, M. Sitarz, P. Jelen, W. Salamon, P. Czaja, J. Jedryka, K. Koronski, A. Kalvane, K. Gornicka, E. Markiewicz, S. Yamashita and Y. Nakazawa, Magnetoelectric, spectroscopic, optical and elastic properties of Co-doped $BaTiO_3$ ceramics, *J. Alloys Compd.*, 2023, **946**, 169344, DOI: 10.1016/j.jallcom.2023.169344.

6 M. Aggarwal, A. K. Singh, G. Sharma, S. Dhiman and S. Kumar, Modulation of polar dynamics with oxygen vacancies in Zn doped $BaZr_{0.1}Ti_{0.9}O_3$, *J. Alloys Compd.*, 2022, **927**, 166957, DOI: 10.1016/j.jallcom.2022.166957.

7 N. V. Dang, N. T. Dung, P. T. Phong and I.-J. Lee, Effect of Fe^{3+} substitution on structural, optical and magnetic properties of barium titanate ceramics, *Phys. B*, 2015, **457**, 103–107, DOI: 10.1016/j.physb.2014.09.046.

8 K. Madhan, C. Jagadeeshwaran and R. Murugaraj, Enhancement of electrical and magnetic properties in acceptor-doped $BaTiO_3$ ferroelectric ceramics, *J. Mater. Sci.: Mater. Electron.*, 2019, **30**, 2953–2965, DOI: 10.1007/s10854-018-00573-6.

9 R. N. Bhowmik, Dielectric and magnetic study of $BaTi_{0.5}Mn_{0.5}O_3$ ceramics, synthesized by solid state sintering, mechanical alloying and chemical routes, *Ceram. Int.*, 2012, **38**, 5069–5080, DOI: 10.1016/j.ceramint.2012.03.009.

10 H. N. H. Nakayama and H. K.-Y. H. Katayama-Yoshida, Theoretical Prediction of Magnetic Properties of $Ba(Ti_{1-x}M_x)O_3$ (M = Sc, V, Cr, Mn, Fe, Co, Ni, Cu), *Jpn. J. Appl. Phys.*, 2001, **40**, L1355, DOI: 10.1143/JJAP.40.L1355.

11 M. S. Alkathy, J. A. Eiras, F. L. Zabotto and K. C. J. Raju, Structural, optical, dielectric, and multiferroic properties of sodium and nickel co-substituted barium titanate ceramics,

J. Mater. Sci.: Mater. Electron., 2021, **32**, 12828–12840, DOI: 10.1007/s10854-020-03900-y.

12 N. Maikhuri, A. K. Panwar and A. K. Jha, Investigation of A- and B-site Fe substituted $BaTiO_3$ ceramics, *J. Appl. Phys.*, 2013, **113**, 17D915, DOI: 10.1063/1.4796193.

13 K. Ito, T. Ichimura, M. Hayashida, T. Nishio, S. Goto, H. Kura, R. Sasaki, M. Tsujikawa, M. Shirai, T. Koganezawa, M. Mizuguchi, Y. Shimada, T. J. Konno, H. Yanagihara and K. Takanashi, Fabrication of L10-ordered FeNi films by denitriding FeNiN(001) and FeNiN(110) films, *J. Alloys Compd.*, 2023, **946**, 169450, DOI: 10.1016/j.jallcom.2023.169450.

14 S. Mehra, R. Pandey, J. Madan, R. Sharma, L. Goswami, G. Gupta, V. N. Singh, A. K. Srivastava and S. N. Sharma, Experimental and Theoretical Investigations of $MAPbX_3$-Based Perovskites (X = Cl, Br, I) for Photovoltaic Applications, *ChemistryOpen*, 2024, **13**, e202300055, DOI: 10.1002/open.202300055.

15 P. Senthilkumar, S. Dhanuskodi, M. Muneeswaran, N. V. Giridharan, S. Kuila and P. N. Vishwakarma, Investigations on the structural, multiferroic, and magnetoelectric properties of $Ba_{1-x}Ce_xTiO_3$, *particles, J. Appl. Phys.*, 2018, **123**, 244101, DOI: 10.1063/1.5019351.

16 Y. Tsur, A. Hitomi, I. Scrymgeour and C. A. Randall, Site Occupancy of Rare-Earth Cations in $BaTiO_3$, *Jpn. J. Appl. Phys.*, 2001, **40**, 255, DOI: 10.1143/JJAP.40.255.

17 H. Kishi, N. Kohzu, J. Sugino, H. Ohsato, Y. Iguchi and T. Okuda, The effect of rare-earth (La, Sm, Dy, Ho and Er) and Mg on the microstructure in $BaTiO_3$, *J. Eur. Ceram. Soc.*, 1999, **19**, 1043–1046, DOI: 10.1016/S0955-2219(98)00370-7.

18 V. Paunovic, L. Zivkovic, L. Vracar, V. Mitic and M. Miljkovic, The effects of additive on microstructure and electrical properties of batio3 ceramics, *Serbian J. Electr. Eng.*, 2004, **1**, 89–98, DOI: 10.2298/SJEE0403089P.

19 D. Lu, M. Toda and M. Sugano, High-Permittivity Double Rare-Earth-Doped Barium Titanate Ceramics with Diffuse Phase Transition, *J. Am. Ceram. Soc.*, 2006, **89**, 3112–3123, DOI: 10.1111/j.1551-2916.2006.00893.x.

20 F. A. Ismail, R. A. M. Osman and M. S. Idris, *Review on dielectric properties of rare earth doped barium titanate*, Penang, Malaysia, 2016, p. 090005, DOI: 10.1063/1.4958786.

21 M. Tihtih, J. E. F. M. Ibrahim, M. A. Basyooni, R. En-nadir, W. Belaid, M. M. Abdelfattah, I. Hussainova, G. Pszota and I. Kocserha, Enhanced optical and thermal conductivity properties of barium titanate ceramic via strontium doping for thermo-optical applications, *Opt. Quantum Electron.*, 2023, **55**, 226, DOI: 10.1007/s11082-022-04516-8.

22 F. A. Rabuffetti, S. P. Culver, J. S. Lee and R. L. Brutchey, Local structural investigation of Eu^{3+}-doped $BaTiO_3$ nanocrystals, *Nanoscale*, 2014, **6**, 2909–2914, DOI: 10.1039/C3NR06610J.

23 H. J. Sumona, Md. S. Sultan, S. A. Urmi and Md. A. Gafur, Investigation of structural, electrical and optical properties of lanthanum and zirconium doped barium titanate ceramics, *Mater. Sci. Eng., B*, 2023, **298**, 116844, DOI: 10.1016/j.mseb.2023.116844.

24 S. N. Rahman, N. Khatun, S. Islam and N. A. Ahmed, International Journal of Emerging Technologies in Computational and Applied Sciences (IJETCAS) https://www.iasir.net, (2014).

25 M. J. Rahman, A. Iffat, A. H. Bhuiyan and S. Choudhury, Alternating current electrical properties of cerium doped barium titanate below the room temperature, *Bangladesh J. Med. Phys.*, 2019, **25**, 55–64.

26 S. N. Rahman, N. Khatun, S. Islam and N. A. Ahmed, International Journal of Emerging Technologies in Computational and Applied Sciences (IJETCAS)https://www.iasir.net, (2014).

27 M. Mostafa, M. J. Rahman and S. Choudhury, Enhanced dielectric properties of $BaTiO_3$ ceramics with cerium doping, manganese doping and Ce–Mn co-doping, *Sci. Eng. Compos. Mater.*, 2019, **26**, 62–69, DOI: 10.1515/secm-2017-0177.

28 S. Yilmaz, B. Kavici, P. Ramakrishnan, C. Celen and B. Amini Horri, Highly Conductive Cerium- and Neodymium-Doped Barium Zirconate Perovskites for Protonic Ceramic Fuel Cells, *Energies*, 2023, **16**, 4318, DOI: 10.3390/en16114318.

29 Y. Liu, X. Deng, J. Chen and Q. Zhou, Preparation and Dielectric Characterization of Ce-Doped $BaTiO_3$ Nanotubes, *IOP Conf. Ser.: Mater. Sci. Eng.*, 2018, **381**, 012104, DOI: 10.1088/1757-899X/381/1/012104.

30 P. Kumar, S. Pathak, K. Jain, A. Singh, Kuldeep, G. A. Basheed and R. P. Pant, Low-temperature large-scale hydrothermal synthesis of optically active PEG-200 capped single domain $MnFe_2O_4$ nanoparticles, *J. Alloys Compd.*, 2022, **904**, 163992.

31 R. H. Buttner and E. N. Maslen, Structural parameters and electron difference density in $BaTiO_3$, *Acta Crystallogr., Sect. B: Struct. Sci.*, 1992, **48**, 764–769, DOI: 10.1107/S010876819200510X.

32 R. Verma, S. Pathak, K. K. Dey, S. Sikarwar, B. C. Yadav and A. K. Srivastava, Facile synthesized zinc oxide nanorod film humidity sensor based on variation in optical transmissivity, *Nanoscale Adv.*, 2022, **4**, 2902–2912.

33 S. Pathak, R. Verma, P. Kumar, A. Singh, S. Singhal, P. Sharma, K. Jain, R. P. Pant and X. Wang, Facile Synthesis, Static, and Dynamic Magnetic Characteristics of Varying Size Double-Surfactant-Coated Mesoscopic Magnetic Nanoparticles Dispersed Stable Aqueous Magnetic Fluids, *Nanomaterials*, 2021, **11**, 3009.

34 A. R. Albuquerque, A. Bruix, I. M. G. Dos Santos, J. R. Sambrano and F. Illas, DFT Study on Ce-Doped Anatase TiO_2: Nature of Ce^{3+} and Ti^{3+} Centers Triggered by Oxygen Vacancy Formation, *J. Phys. Chem. C*, 2014, **118**, 9677–9689, DOI: 10.1021/jp501757f.

35 S. Pathak, R. Verma, S. Singhal, R. Chaturvedi, P. Kumar, P. Sharma, R. P. Pant and X. Wang, Spin dynamics investigations of multifunctional ambient scalable Fe_3O_4 surface decorated ZnO magnetic nanocomposite using FMR, *Sci. Rep.*, 2021, **11**, 3799.

36 S. Pathak, K. Jain, P. Kumar, X. Wang and R. P. Pant, Improved thermal performance of annular fin-shell tube storage system using magnetic fluid, *Appl. Energy*, 2019, **239**, 1524–1535.

37 A. Singh, P. Kumar, S. Pathak, K. Jain, P. Garg, M. Pant, A. K. Mahapatro, D. Rath, L. Wang, S.-K. Kim, K. K. Maurya and R. P. Pant, A threefold increase in SAR performance for magnetic hyperthermia by compositional tuning in zinc-substituted iron oxide superparamagnetic nanoparticles with superior biocompatibility, *J. Alloys Compd.*, 2023, **968**, 171868.

38 P. Kumar, S. Pathak, A. Singh, K. Jain, H. Khanduri, L. Wang, S.-K. Kim and R. P. Pant, Observation of intrinsic fluorescence in cobalt ferrite magnetic nanoparticles by Mn^{2+} substitution and tuning the spin dynamics by cation distribution, *J. Mater. Chem. C*, 2022, **10**, 12652–12679.

39 A. Singh, P. Kumar, S. Pathak, K. Jain, P. Garg, M. Pant, A. K. Mahapatro, R. K. Singh, P. Rajput and S.-K. Kim, Tailored nanoparticles for magnetic hyperthermia: Highly stable aqueous dispersion of Mn-substituted magnetite superparamagnetic nanoparticles by double surfactant coating for improved heating efficiency, *J. Alloys Compd.*, 2024, **976**, 172999.

40 P. Senthilkumar, S. Dhanuskodi, M. Muneeswaran, N. V. Giridharan, S. Kuila and P. N. Vishwakarma, Investigations on the structural, multiferroic, and magnetoelectric properties of $Ba_{1-x}Ce_xTiO_3$ particles, *J. Appl. Phys.*, 2018, **123**, 244101, DOI: **10.1063/1.5019351**.

41 A. Rana, S. Pathak, K. Kumar, A. Kumari, S. Chopra, M. Kumar, D. Kamil, R. Srivastava, S.-K. Kim and R. Verma, Multifaceted properties of TiO 2 nanoparticles synthesized using Mangifera indica and Azadirachta indica plant extracts: antimicrobial, antioxidant, and non-linear optical activity investigation for sustainable agricultural applications, *Mater. Adv.*, 2024, **5**, 2767–2784.

42 M. Kumar, S. Rani, A. Kumar, J. Tawale, R. Srivastava, B. P. Singh, S. Pathak, X. Wang and V. N. Singh, Broadband (NIR-Vis-UV) photoresponse of annealed SnSe films and effective oxidation passivation using Si protective layer, *Mater. Res. Bull.*, 2022, **153**, 111913.

43 U. D. Venkateswaran, V. M. Naik and R. Naik, High-pressure Raman studies of polycrystalline $BaTiO_3$, *Phys. Rev. B: Condens. Matter Mater. Phys.*, 1998, **58**, 14256–14260, DOI: **10.1103/PhysRevB.58.14256**.

44 Y. Shiratori, C. Pithan, J. Dornseiffer and R. Waser, Raman scattering studies on nanocrystalline $BaTiO_3$ Part I---isolated particles and aggregates, *J. Raman Spectrosc.*, 2007, **38**, 1288–1299, DOI: **10.1002/jrs.1764**.

45 L. Ju, T. Sabergharesou, K. G. Stamplecoskie, M. Hegde, T. Wang, N. A. Combe, H. Wu and P. V. Radovanovic, Interplay between Size, Composition, and Phase Transition of Nanocrystalline Cr^{3+}-Doped $BaTiO_3$ as a Path to Multiferroism in Perovskite-Type Oxides, *J. Am. Chem. Soc.*, 2012, **134**, 1136–1146, DOI: **10.1021/ja2091678**.

46 Noorjahan, G. A. Basheed, K. Jain, S. Pathak and R. P. Pant, Dipolar Interaction and Magneto-Viscoelasticity in Nanomagnetic Fluid, *J. Nanosci. Nanotechnol.*, 2018, **18**, 2746–2751.

47 Mst S. Mostari, N. Islam and Md. A. Matin, Structural modification and evaluation of dielectric and ferromagnetic properties of Ce-modified $BiFeO_3$–$BaTiO_3$ ceramics, *Ceram. Int.*, 2020, **46**, 15840–15850, DOI: **10.1016/j.ceramint.2020.03.131**.

48 A. Rani, J. Kolte and P. Gopalan, Structural, electrical, magnetic and magnetoelectric properties of Co-doped $BaTiO_3$ multiferroic ceramics, *Ceram. Int.*, 2018, **44**, 16703–16711, DOI: **10.1016/j.ceramint.2018.06.098**.

49 P. Kumar, S. Pathak, K. Jain, A. Singh, Kuldeep, G. A. Basheed and R. P. Pant, Low-temperature large-scale hydrothermal synthesis of optically active PEG-200 capped single domain $MnFe_2O_4$ nanoparticles, *J. Alloys Compd.*, 2022, **904**, 163992, DOI: **10.1016/j.jallcom.2022.163992**.

50 P. Kumar, H. Khanduri, S. Pathak, A. Singh, G. A. Basheed and R. P. Pant, Temperature selectivity for single phase hydrothermal synthesis of PEG-400 coated magnetite nanoparticles, *Dalton Trans.*, 2020, **49**, 8672–8683.

51 A. Singh, S. Pathak, P. Kumar, P. Sharma, A. Rathi, G. A. Basheed, K. K. Maurya and R. P. Pant, Tuning the magnetocrystalline anisotropy and spin dynamics in $Co_xZn_{1-x}Fe_2O_4$ $(0 \leq x \leq 1)$ nanoferrites, *J. Magn. Magn. Mater.*, 2020, **493**, 165737.

52 D. Cao, M. Q. Cai, Y. Zheng and W. Y. Hu, First-principles study for vacancy-induced magnetism in nonmagnetic ferroelectric $BaTiO_3$, *Phys. Chem. Chem. Phys.*, 2009, **11**, 10934, DOI: **10.1039/b908058a**.

53 S. R. Singamaneni, S. Punugupati, J. T. Prater, F. Hunte and J. Narayan, Ferroelectric and ferromagnetic properties in BaTiO3 thin films on Si (100), *J. Appl. Phys.*, 2014, **116**, 094103, DOI: **10.1063/1.4894508**.

54 S. Majumder, P. Basera, M. Tripathi, R. J. Choudhary, S. Bhattacharya, K. Bapna and D. M. Phase, Elucidating the origin of magnetic ordering in ferroelectric $BaTiO_3$-d thin film via electronic structure modification, *J. Phys.: Condens. Matter*, 2019, **31**, 205001, DOI: **10.1088/1361-648X/ab06d5**.

55 B. Gao and Q. Xu, Construction of Long-Range Magnetic Sequences on Different Surfaces of $BaTiO_3$, *ChemPhysChem*, 2023, **24**, e202200559, DOI: **10.1002/cphc.202200559**.

56 P. Kumar, S. Pathak, A. Singh, Kuldeep, H. Khanduri, X. Wang, G. A. Basheed and R. P. Pant, Optimization of cobalt concentration for improved magnetic characteristics and stability of $Co_xFe_{3-x}O_4$ mixed ferrite nanomagnetic fluids, *Mater. Chem. Phys.*, 2021, 124476.

57 P. Kumar, S. Pathak, A. Singh, H. Khanduri, K. Jain, J. Tawale, L. Wang, G. Basheed and R. Pant, Enhanced static and dynamic magnetic properties of PEG-400 coated $CoFe_{2-x}Er_xO_4$ $(0.7 \leq x \leq 0)$ nanoferrites, *J. Alloys Compd.*, 2021, **887**, 161418.

58 B. Bhushan, Z. Wang, J. Tol, N. S. Dalal, A. Basumallick, N. Y. Vasanthacharya, S. Kumar and D. Das, Tailoring the Magnetic and Optical Characteristics of Nanocrystalline $BiFeO_3$ by Ce Doping, *J. Am. Ceram. Soc.*, 2012, **95**, 1985–1992, DOI: **10.1111/j.1551-2916.2012.05132.x**.

59 P. Dutta, S. Pal, M. S. Seehra, Y. Shi, E. M. Eyring and R. D. Ernst, Concentration of Ce^{3+} and Oxygen Vacancies in Cerium Oxide Nanoparticles, *Chem. Mater.*, 2006, **18**, 5144–5146, DOI: **10.1021/cm061580n**.

60 P. Mohanapriya, R. Pradeepkumar, N. Victor Jaya and T. S. Natarajan, Magnetic and optical properties of electrospun hollow nanofibers of SnO_2 doped with Ce-ion, *Appl. Phys. Lett.*, 2014, **105**, 022406, DOI: 10.1063/1.4886804.

61 H. Yue, K. Fang, T. Chen, Q. Jing, K. Guo, Z. Liu, B. Xie, P. Mao, J. Lu, F. E. H. Tay, I. Tan and K. Yao, First-Principle Study on Correlate Structural, Electronic and Optical Properties of Ce-Doped $BaTiO_3$, *Crystals*, 2023, **13**, 255, DOI: 10.3390/cryst13020255.

62 P. Victor, R. Ranjith and S. B. Krupanidhi, Normal ferroelectric to relaxor behavior in laser ablated Ca-doped barium titanate thin films, *J. Appl. Phys.*, 2003, **94**, 7702–7709.

63 C. Ang, Z. Yu, Z. Jing, R. Guo, A. S. Bhalla and L. E. Cross, Piezoelectric and electrostrictive strain behavior of Ce-doped $BaTiO_3$ ceramics, *Appl. Phys. Lett.*, 2002, **80**, 3424–3426, DOI: 10.1063/1.1473871.

64 P. Esther Rubavathi, M. Veera Gajendra Babu, B. Bagyalakshmi, L. Venkidu, D. Dhayanithi, N. V. Giridharan and B. Sundarakannan, Impact of Ba/Ti ratio on the magnetic properties of $BaTiO_3$ ceramics, *Vacuum*, 2019, **159**, 374–378, DOI: 10.1016/j.vacuum.2018.10.063.

65 G. Park, H. Jo, Y.-J. Oh, S. Pathak and S.-K. Kim, Magnetization Reversals in Magnetosome Linear-Chain Assemblies Extracted from Magnetotactic Bacteria: An Experimental and Micromagnetic Simulation Study, *J. Mater. Chem. C*, 2023, **11**(29), 9794–9803.

66 P. Kumar, S. Pathak, A. Singh, H. Khanduri, G. Basheed, L. Wang and R. Pant, Microwave spin resonance investigation on the effect of the post-processing annealing of $CoFe_2O_4$ nanoparticles, *Nanoscale Adv.*, 2020, **2**, 1939–1948.

67 S. Pathak, H. An and S.-K. Kim, Dual-Cross-Linked Superparamagnetic Hydrogels with Tailored Viscoelasticity for Soft Robotics, *ACS Appl. Nano Mater.*, 2024, **7**(15), 17482–17492.

68 R. Singh, S. Pathak, K. Jain, Noorjahan and S.-K. Kim, Correlating the Dipolar Interactions Induced Magneto-Viscoelasticity and Thermal Conductivity Enhancements in Nanomagnetic Fluids, *Small*, 2023, **19**(39), 2205741.

69 K. L. Routray, S. Saha and D. Behera, Nanosized $CoFe_2O_4$-graphene nanoplatelets with massive dielectric enhancement for high frequency device application, *Mater. Sci. Eng., B*, 2020, **257**, 114548.

70 H.-I. Hsiang, C.-S. Hsi, C.-C. Huang and S.-L. Fu, Sintering behavior and dielectric properties of $BaTiO_3$ ceramics with glass addition for internal capacitor of LTCC, *J. Alloys Compd.*, 2008, **459**, 307–310, DOI: 10.1016/j.jallcom.2007.04.218.

71 C. G. Koops, On the Dispersion of Resistivity and Dielectric Constant of Some Semiconductors at Audiofrequencies, *Phys. Rev.*, 1951, **83**, 121–124, DOI: 10.1103/PhysRev.83.121.

72 J. C. Maxwell, Electrolytic polarization, *Electr. Magn.*, 1929, **1**, 328.

73 T. Prodromakis and C. Papavassiliou, Engineering the Maxwell–Wagner polarization effect, *Appl. Surf. Sci.*, 2009, **255**, 6989–6994, DOI: 10.1016/j.apsusc.2009.03.030.

74 S. Choudhury, M. Hakim, Md. A. Bhuiyan, M. J. Rahman and S. Yasmin, Dielectric and Structural Properties of Pure and Cerium Doped $BaTiO_3$, 2009.

75 P. Sarah and S. V. Suryanarayana, Dielectric properties of piezoelectric 3-0 composites of lithium ferrite/barium titanate, *Bull. Mater. Sci.*, 2003, **26**, 745–747, DOI: 10.1007/BF02706773.

76 K. L. Routray and S. Saha, Investigation of structural, electrical, and magnetic variations of Ni–Zn–Co ferrites by substituting rare earth Ho^{3+} for high-frequency applications, *Phys. Scr.*, 2024, **99**, 055950, DOI: 10.1088/1402-4896/ad3ae0.

77 A. Parveez, M. S. Shekhawat, F. Nayeem, S. S. Mohd, R. R. Sinha and S. A. Khader, *Dielectric and conductivity studies of Co–Cu mixed ferrite*, Bikaner, India, 2018, p. 030284. , DOI: 10.1063/1.5032619.

78 K. L. Routray, S. Saha and D. Behera, Insight Into the Anomalous Electrical Behavior, Dielectric and Magnetic Study of Ag-Doped $CoFe_2O_4$ Synthesised by Okra Extract-Assisted Green Synthesis, *J. Electron. Mater.*, 2020, **49**, 7244–7258, DOI: 10.1007/s11664-020-08468-1.

79 S. Saha and K. L. Routray, Structural, magnetic and dielectric properties of Terbium substituted nanosized Nickel-Ferrites from a new perspective, *J. Sol-Gel Sci. Technol.*, 2024, **111**, 566–585, DOI: 10.1007/s10971-024-06465-y.

80 K. L. Routray, S. Saha and D. Behera, Effect of CNTs blending on the structural, dielectric and magneticproperties of nanosized cobalt ferrite, *Mater. Sci. Eng., B*, 2017, **226**, 199–205.

81 K. L. Routray and S. Saha, Graphene nanoplatelets anchored into Ag doped spinel $CoFe_2O_4$ nanohybrid: Synthesis, structural, electrical, superior dielectric and room temperature induced ferromagnetism performance for high frequency device application, *Diamond Relat. Mater.*, 2024, **141**, 110680.

82 S. Saha, N. Das, P. Chakra, K. L. Routray and D. Behera, Role of graphene on structural, dielectric and magnetic properties of $CoFe_2O_4$ nanoparticles, *J. Mater. Sci.: Mater. Electron.*, 2019, **30**, 14464–14479.

83 S. Saha and K. L. Routray, Structural, magnetic and dielectric properties of Terbium substituted nanosized Nickel-Ferrites from a new perspective, *J. Sol-Gel Sci. Technol.*, 2024, 1–20.